This is a repository copy of *Deformation behaviour of a FAST diffusion bond processed from dissimilar titanium alloy powders*.

White Rose Research Online URL for this paper:
https://eprints.whiterose.ac.uk/174755/

Version: Published Version

Article:
Levano Blanch, O., Lunt, D., Baxter, G.J. et al. (1 more author) (2021) Deformation behaviour of a FAST diffusion bond processed from dissimilar titanium alloy powders. Metallurgical and Materials Transactions A: Physical Metallurgy and Materials Science, 52. pp. 3064-3082. ISSN 1073-5623

https://doi.org/10.1007/s11661-021-06301-w

Reuse
This article is distributed under the terms of the Creative Commons Attribution (CC BY) licence. This licence allows you to distribute, remix, tweak, and build upon the work, even commercially, as long as you credit the authors for the original work. More information and the full terms of the licence here: https://creativecommons.org/licenses/

Takedown
If you consider content in White Rose Research Online to be in breach of UK law, please notify us by emailing eprints@whiterose.ac.uk including the URL of the record and the reason for the withdrawal request.

eprints@whiterose.ac.uk
https://eprints.whiterose.ac.uk/

ORIGINAL RESEARCH ARTICLE

Deformation Behaviour of a FAST Diffusion Bond Processed from Dissimilar Titanium Alloy Powders

OLIVER LEVANO BLANCH, DAVID LUNT, GAVIN J. BAXTER, and MARTIN JACKSON

Titanium alloys have a high strength-to-weight ratio, fatigue performance and excellent corrosion resistance, and therefore are widely used in the aerospace sector due to their ability to withstand severe mechanical and thermal stresses in service. There are numerous cases where it would be desirable to use different titanium alloys in defined subcomponent regions to improve performance and efficiency. Conventional processing routes do not permit components to be produced with multiple titanium alloys and thus, design efficiency and optimization of component properties is compromised or over-engineered. In this study, a hybrid solid-state consolidation route is presented whereby field assisted sintering technology (FAST) is exploited to diffusion bond (DB) dissimilar titanium alloy powders in defined regions—a process termed FAST-DB. Titanium alloy powders Ti-6Al-4V (Ti-64) and Ti-6Al-2Sn-4Zr-2Mo (Ti-6242) were bonded using FAST in order to study the tensile deformation behavior and strain localization across a dissimilar alloy solid-state bond. FAST-DB was carried out at the sub- and super- beta transus temperatures of both alloys to generate dissimilar microstructure morphologies across the bond. In all cases, diffusion bonds showed excellent structural integrity with no defects and a smooth hardness profile across the bond. The deformation characteristics of the bonds was studied using two different tensile test approaches. The first approach used ASTM standard specimens to measure the mechanical properties of FAST-DB samples and study the location of the tensile failure. The second approach used a microtester and optical Digital Image Correlation to capture the grain interaction in the bond region under tensile loading. The work demonstrated that the diffusion bond remains intact and that tensile failure occurs in Ti-64 (i.e. the lower strength alloy) and is independent of the grain crystal orientation. The results from this study will provide materials engineers confidence in nesting FAST-DB technology in future near net shape manufacturing routes.

https://doi.org/10.1007/s11661-021-06301-w
© The Author(s) 2021

I. INTRODUCTION

TITANIUM alloys are widely used in the aerospace sector due to their high strength-to-weight ratio, corrosion resistance and ability to operate at relatively high temperatures.[1–4] For example, 25-30 pct of the weight of a gas turbine aero-engine is made up of titanium alloys such as Ti-6Al-4V (Ti-64), Ti-6Al-2Sn-4Zr-2Mo (Ti-6242) and Ti-6Al-2Sn-4Zr-6Mo (Ti-6246).[2] One of the issues with manufacturing in titanium, that restricts it largely to the aerospace sector is the high processing cost and the high Buy-to-Fly ratio (BTF), which can exceed 10:1.[5] Aerospace titanium alloy components used in demanding environments require a good combination of creep and fatigue resistance, yet are designed and manufactured from a single titanium alloy with a similar microstructure and set of properties in different subcomponent regions. The performance of titanium components could be improved by using a tailored creep resistant or fatigue resistant titanium alloy in defined subcomponent regions. The ability to manufacture a component with dissimilar alloys in site-specific, subcomponent regions would enable designers to optimize the performance of titanium forged components. The greatest challenge for materials engineers is to determine the appropriate technology (and whether it exists) to reliably join both alloys and to ensure that the bond does not compromise the structural integrity of the component. Additionally, there is a drive to move towards near-net shape manufacturing with low

OLIVER LEVANO BLANCH and MARTIN JACKSON are with the Department of Materials Science and Engineering, The University of Sheffield, Sir Robert Hadfield Building, Sheffield S1 3JD, UK. Contact e-mail: o.levano@sheffield.ac.uk DAVID LUNT is with the School of Materials, The University of Manchester, Oxford Road, Manchester, M13 9PL, UK. GAVIN J. BAXTER is with the Rolls-Royce plc, PO Box 31, Derby DE24 8EJ, UK.

Manuscript submitted December 14, 2020; accepted April 19, 2021. Article published online May 17, 2021

material wastage in order to reduce the excessive BTF of titanium aerospace parts.

An ideal candidate to create a near-net shape multi-titanium alloy component and reduce the BTF value is the solid-state powder consolidation technology known as spark plasma sintering (SPS) or field assisted sintering technology (FAST). FAST uses pulsed electrical current and mechanical pressure through graphite dies to fully consolidate powder into a shaped part. Dissimilar powders can be distributed into the graphite die with a degree of accuracy to obtain the multi-alloy components with alloys in site-specific regions. The advantages of FAST, in relation to conventional techniques, is that it can retain small grain sizes due to the high heating rates obtained with the Joule heating effect and it requires lower temperatures and dwell times to obtain a fully consolidated part.[6–9] There are three multi-physical parameters involved in the FAST process: electric current, voltage and pressure.[8] It has been observed that the electric current improves metal powder densification by the electromigration phenomenon, yet temperature still has the most dominant effect on densification.[10] Trzaska *et al.*[11] also observed enhanced densification during the FAST of metal powders due to high dislocation densities and diffusion rates at interparticle contact regions. Additionally, previous studies have demonstrated an enhancement in diffusion when pulsed current is used.[12,13] In 2014, a short review by Kelly and Graeve[14] concluded that FAST/SPS was cheaper than conventional powder metallurgy processes such as hot pressing (HP). Since then, FAST has been shown to be capable of creating shaped parts in one step[15–18] or can be combined with hot forging to obtain near-net shaped parts with as-forged properties in two steps (and termed FAST-*forge*).[19–22] Using FAST provides sustainable processing opportunities; titanium alloy powder and waste particulates (such as machining swarf) can be fully consolidated into pre-forging billets or final parts in one or two solid-state steps. This could lead to significant cost reductions in titanium alloy component manufacture compared to the conventional multi-step route.[23]

To date, the diffusion bonds obtained using FAST produce a graded transition region between titanium alloys of the order of 300-500 μm[24] with the advantage that there is no resultant heat affected zone from the solid-state process. An example of a bond produced by FAST is shown in Figure 1, where a chemically graded grain exists at the diffusion bond region. At higher magnification, there is a gentle transition from Ti-64 to Ti-6242 due to the change in Z contrast from the darker alpha laths in Ti-64 to brighter (more heavily stabilized) alpha laths in Ti-6242, but with the no noticeable difference morphology. There has been limited research focused on joining titanium alloys using FAST technology: He *et al.*[25] joined two solid blocks of Ti-64 with FAST and HP under several conditions and tested the strength of the bond with tensile tests. The failure points of the FAST joints occurred in the base material when processed at the highest temperatures. The FAST specimens achieved superior mechanical properties than the joints produced using HP for most of the conditions. Miriyev *et al.*[26] joined solid Ti-64 with AISI4330 steel achieving a tensile strength of 250 MPa in the joint. Kumar *et al.*[27] investigated similar flat bonds between commercially pure Ti (CP-Ti) and AISI304L using FAST, where an average strength of 260 MPa was recorded. However, when threads were incorporated into the bond, the average strength increased to 400 MPa. The main issue observed during the bonding of titanium to steel was the formation of intermetallic phases that produced a brittle failure in the bond region during mechanical testing. Pripanapong *et al.*[28,29] used FAST to join solid CP-Ti with magnesium alloys, achieving a tensile bond efficiency of 96 pct in relation to the bulk material. This efficiency was obtained when the Al content was increased, as it led to the precipitation of Ti_3Al, which locally increased the strength of the bond region. Zhao *et al.*[30] joined solid TiAl preforms using FAST and observed that the strength of the bond increased when the processing temperature increased due to the higher levels of diffusion. Nevertheless, the strength of the bond decreased when the pressure was increased due to recrystallization and grain growth.

Pope *et al.*[24] pioneered the use of FAST to diffusion bond dissimilar titanium alloy powders (termed FAST-DB), in combinations of Ti-64/Ti-5553 and Ti-64/CP-Ti into fully consolidated samples and demonstrated that the failure occurred in the lower strength alloy during uniaxial tensile loading. Although FAST has been well characterized as an effective process to bond dissimilar titanium alloys to form ''architectural'' microstructures,[21,22,31,32] there has been limited research into the deformation mechanism and strain localization in the diffusion bond region during tensile loading, which is a key focus of this paper.

In the hexagonal close-packed (HCP) titanium alloys, the easiest slip modes occur along the $<11\bar{2}0>$ direction for basal $\{0001\}$ and prismatic $\{10\bar{1}0\}$ planes. Additionally, $\vec{c}+\vec{a}$ slip occurs on the $\{10\bar{1}1\}$ and $\{10\bar{2}2\}$ pyramidal planes.[33–35] This type of slip is more difficult than $\vec{a}$ slip at room temperature.[3,4] The activation of a slip system for a single crystal is dependent on the grain orientation relative to the loading direction, which is represented with the Schmid factor (m), and the critical resolved shear stress (CRSS) of the slip system.[36] For polycrystalline materials the interaction between neighboring grains has to be taken into account and it has been suggested that is necessary to add a hardening effect to the CRSS value.[37] The pyramidal CRSS for Ti-64 is often considered to be at least two times higher than the prismatic CRSS, and thought to be up to thirteen times higher for CP-Ti with a low oxygen content.[38] Furthermore, the CRSS for the prismatic and basal plane is thought to be ~ 1:1, but it has been observed in tensile and compressive tests for single grain and textured titanium alloys that the prismatic plane tend to have a lower value.[33,39, 40] Although the global Schmid factor calculation does not take into account the local stress state, it has been found by Bridier *et al.*[40] to be an adequate parameter for determining the active slip mode in Ti-64, i.e., with the activated slip systems corresponding to the those with the highest Schmid

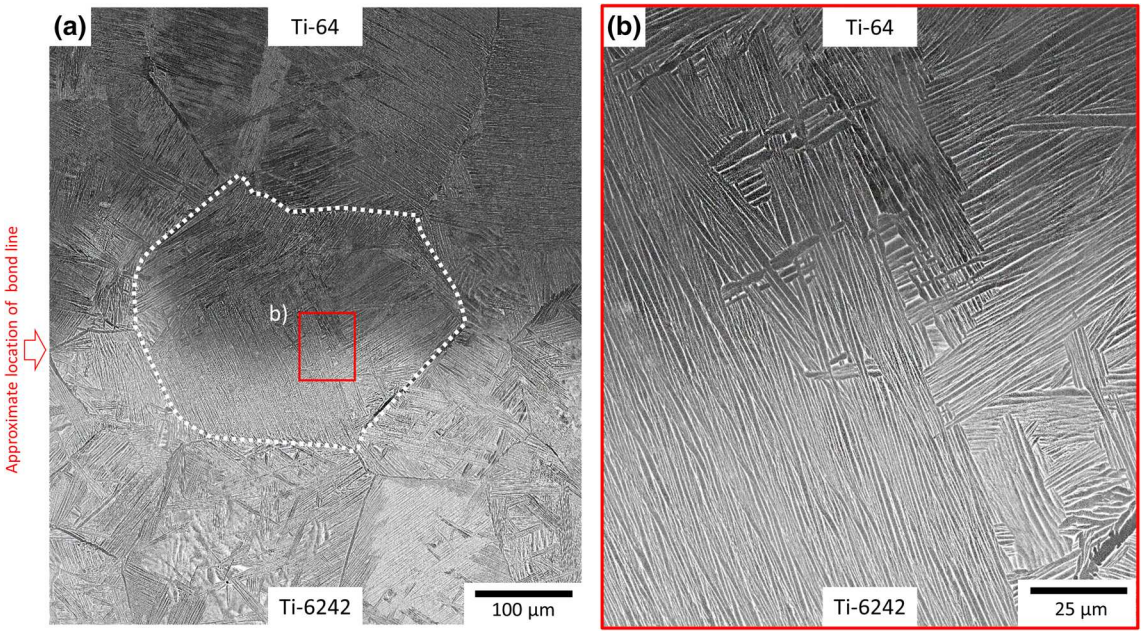

Fig. 1—Backscattered electron micrographs of the FAST-DB bond between Ti-6242 and Ti-64; (*a*) Micrograph illustrating chemical grading across a grain at the diffusion bond region—the red arrow shows the approximate location of the bond. (*b*) Higher resolution micrograph of the diffusion bond and similar alpha colony morphology across the diffusion bond region.

factor. However, recent high-resolution studies have shown that there is often more complex deformation occurring at the subgrain scale.[41]

In this study, optical Digital Image Correlation (DIC) is used to characterize the deformation of the diffusion bond region between Ti-64 and Ti-6242 under tensile loading at different length scales. DIC is a useful tool that can be used to map the local strain of a specimen through images.[42–45] The DIC technique works by tracking surface features while applying deformation and comparing the location of these features to their initial position. With optical DIC it is possible to quantify the strain localization at a mesoscale level. For example, Littlewood *et al.*[46] and Lunt *et al.*[47,48] used optical DIC in a forged Ti-64 specimen and a Ti-64 plasma wire deposition specimen to observe the effective strain of the grains and strain partitioning between neighboring grains of different crystallographic orientations.

The aim of this work is to assess the mechanical performance under uniaxial tensile strength of the FAST-DB joint between Ti-64 and Ti-6242 after subtransus and supertransus FAST processing.

II. METHODOLOGY

This work presents two separate sets of experiments: one analyses the performance of the bond in a standard tensile test sample in both the subtransus and supertransus FAST processed condition. The second experiment uses optical DIC (higher resolution) to further understand the effect of the bond for supertransus conditions. The standard tensile test samples were machined from two separated FAST-DB discs of 250 mm diameter while the optical DIC samples were machined from one FAST-DB disc of 60 mm diameter.

A. *Titanium Alloy Powders*

The titanium powder alloys used in this study were Ti-6Al-4V (Ti-64) and Ti-6Al-2Sn-4Zr-2Mo (Ti-6242). The morphology and microstructure of the powders are shown in Figure 2, where the nomenclature (S) and (D) has been added after the type of alloy to differentiate the powders used in the standard tensile test (S) and the optical DIC test (D). The top row of Figure 2 shows that Ti-6242 powder has a greater fraction of fine powder "satellites" and a higher frequency of particles partially melted compared to the Ti-64 powder. For Ti-6242 (S), it was observed the formation of fused powder joined together, which is typically observed in recycled titanium powder that has been previously used in additive manufacturing processes. A martensitic microstructure is observed for all the powders in the middle row of Figure 2 due to the rapid cooling rates during powder production. The powder's aspect ratio, circularity and porosity were characterized using the optical microscope Olympus Bx51 with the software Clemex Vision PE image analysis system. The powder was cold mounted with epoxy-resin, followed by a short grinding and polishing. Then, the software Clemex Vision PE analyzed more than 20,000 powder particles for each powder type. The last row of Figure 2 shows the probability density of the powder as a function of the aspect ratio, circularity and the diameter of the powder. A perfect sphere will have value of aspect ratio and circularity of 1. Therefore, the Y axis represents the multiplication between the aspect ratio and the

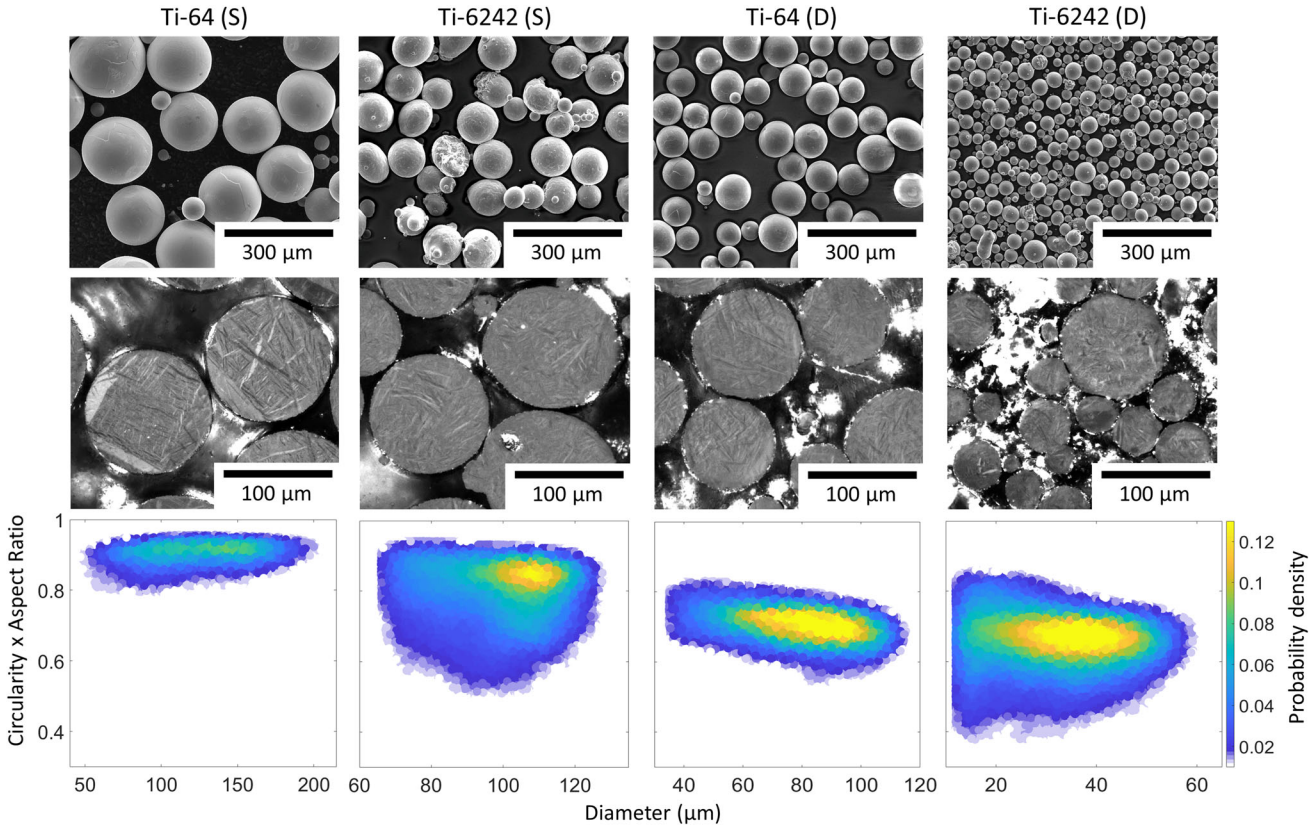

Fig. 2—Micrographs and graphs showing the characteristics of the four powders used. The first row is made of secondary electron micrographs of the external appearance of the powder. The middle row are light micrographs of the powder microstructure under cross polarized light. The bottom row presents density plots of the aspect ratio and the circularity of the powder as a function of the diameter.

circularity because it shows how close to a perfect sphere the powder particle is. It is observed that the Ti-64 powder has more particles closer to a perfect sphere than the Ti-6242 powder, which correlates well with the SEM micrographs from the first row of Figure 2.

The particle size distribution (PSD) was measured using a Malvern Mastersizer 3000 laser diffraction particle size analyzer with a wet dispersion method. A total of 20 repetitions were conducted for each powder and the distributions can be found in Table I. Additionally, Table I shows the porosity measured with the software Clemex for each powder type. The chemical composition of the elements were measured by X-EDS, XRF (Bed Fusion) and LECO analysis and the results are shown in Table II.

B. *FAST Processing and Test Sample Manufacture*

Two different tensile samples were made for different levels of mechanical assessment: one ASTM E8/E8M tensile specimen[49] was machined for a standard tensile test and a smaller bespoke tensile specimen was machined in order to study the deformation characteristics in the diffusion bond region. Table III shows the different tensile samples tested in this study and the FAST processing dwell temperature used for each one. The applied pressure of 32.5 MPa was used for all samples.

Figure 3 presents the steps to manufacture the standard tensile test samples which were processed on an FCT System GmbH FAST Furnace Type H-HP D 250. The FAST furnace is capable of producing discs with a diameter of 250 mm and the temperature is measured with a pyrometer at the interface between the powder and the upper graphite ram. The powder was separated in the graphite ring by aluminum dividers, as shown in Figure 3(a) and the two alloy powders were distribution as schematically illustrated in Figure 3(c). Once the graphite ring was filled with the two powders, the dividers were carefully removed, leaving a straight interface between the two powders. The powder was fully consolidated in the FAST furnace to create a disc with a diameter of 250 mm and a thickness of 30 mm. To prevent oxidation of the titanium sample, the process was carried out under vacuum.

In this study, a total of two discs with the same alloy distribution were processed at two different temperatures with respect to the β transus of both Ti-64 and Ti-6242, which is approximately 995 °C: FAST processing was conducted at dwell temperatures of 970 °C and 1030 °C, which were respectively in the subtransus and supertransus phase regions for both alloys also. The surface of the FAST discs were then skimmed in order to accurately locate the bond line between the two alloys. The diffusion bonding was so effective that it was challenging to visually locate the bond between these

Table I. Particle Size Distribution and Porosity of the Titanium Alloy Powders

Test	Disc	Powder	Dx (10) (μm)	Dx (50) (μm)	Dx (90) (μm)	Porosity (pct)
Standard Tensile Test	disc 1 and 2	Ti-64 (S)	93	160	299	0.05
		Ti-6242 (S)	93.5	113	137	0.41
Optical DIC Test	disc 3	Ti-64 (D)	61.3	86.7	123	0.07
		Ti-6242 (D)	25.2	37.4	53.7	0.06

Table II. Chemical Composition of the Four Titanium Alloy Powders Represented in Pct

Powder	Ti	Al	V	Sn	Zr	Mo	Fe	Si	C	S	O	N	H*
Ti-64 (S)	bal.	6.16	3.86	—	—	—	0.26	—	0.028	0.01	0.163	0.019	29
Ti-6242 (S)	bal.	5.74	—	2.22	4.58	2.32	<0.05	<0.05	0.04	0.01	0.118	0.008	19
Ti-64 (D)	bal.	6.02	3.66	—	—	—	0.16	—	0.023	0.01	0.181	0.003	32
Ti-6242 (D)	bal.	5.69	—	1.89	4.41	1.93	0.05	0.09	0.07	0.01	0.148	0.002	21

H* is represented in parts per million (PPM).

Table III. Samples Produced with FAST and the Corresponding Processing Temperatures

Test	Disc	Disc Diameter (mm)	Processing Conditions	Temperature (°C)	Name	Material
Standard Tensile Test	disc 1	250	subtransus	970	T1	Ti-6242
					TDB1	Ti-64/Ti-6242
	disc 2		supertransus	1030	T2	Ti-6242
					TDB2	Ti-64/Ti-6242
Optical DIC Analysis	disc 3	60	supertransus	1030	TDIC	Ti-64/Ti-6242

two alloys. A range of samples were machined, including tensile samples from the two FAST-DB discs, as shown in Figure 3(c).

The tensile samples for the optical Digital Image Correlation (DIC) test were produced on the smaller FCT System GmbH FAST Furnace Type HP D 25. Figure 4 shows the procedure followed to produce the samples for the optical DIC test. The temperature was also measured at the interface between the powder and the upper graphite ram with an axial pyrometer. The diameter of the graphite ring was 60 mm and the walls of the ring were covered with graphite foil to avoid the powder sticking in the graphite ring. A 3D printed polymer cross-shaped divider was used to separate the powders, as shown in Figure 4(a). The divider maintained a straight interface between the two alloy powders when slowly removed from the graphite ring. For this sample, half of the graphite ring was filled with Ti-64 powder and the other half was filled with Ti-6242 powder. The powder was processed under vacuum conditions to avoid any oxidation and the process temperatures are shown in Table III.

The tensile sample used was a double bone design and was 50 mm long, as shown in Figure 4(c)—this design was used to constrain the location of the deformation. In order to locate the bond in the FAST disc, the surface was lightly ground using SiC paper until the bond was visible and the tensile samples were subsequently machined with the diffusion bond in the central region (Figure 4(c)).

C. *Standard Tensile Testing*

As Table III shows, two discs were processed at the dwell temperatures of 970 °C (subtransus) and 1030 °C (supertransus). For each disc, samples were extracted using wire EDM and finish machined to ASTM E8/E8M[49] specifications. As Figure 3(c) depicts, from each FAST disc, four tensile specimens were extracted entirely from the Ti-6242 region and four tensile samples were extracted across the bond region between Ti-64 and Ti-6242 (Figure 3(d)). Before testing, one face of the tensile test samples was ground and polished to a mirror finish so the bond could be tracked during the tensile test. The tensile test was carried out using a Tinius Olsen 25 ST benchtop tester and LabView software was used to record the force and displacement of the sample. The force was read directly from the tester and the displacement was read from an Epsilon Axial Extensometer–Model 3542 with a gauge length of 50 mm. The cross-head was set to a constant displacement of 0.01 mm/s and the test stopped when the sample failed.

For one TDB1 sample and one TDB2 sample, a GOM ARAMIS 3D system was used to measure the deformation of the sample with the DIC technique. The data obtained was post analyzed with the GOM

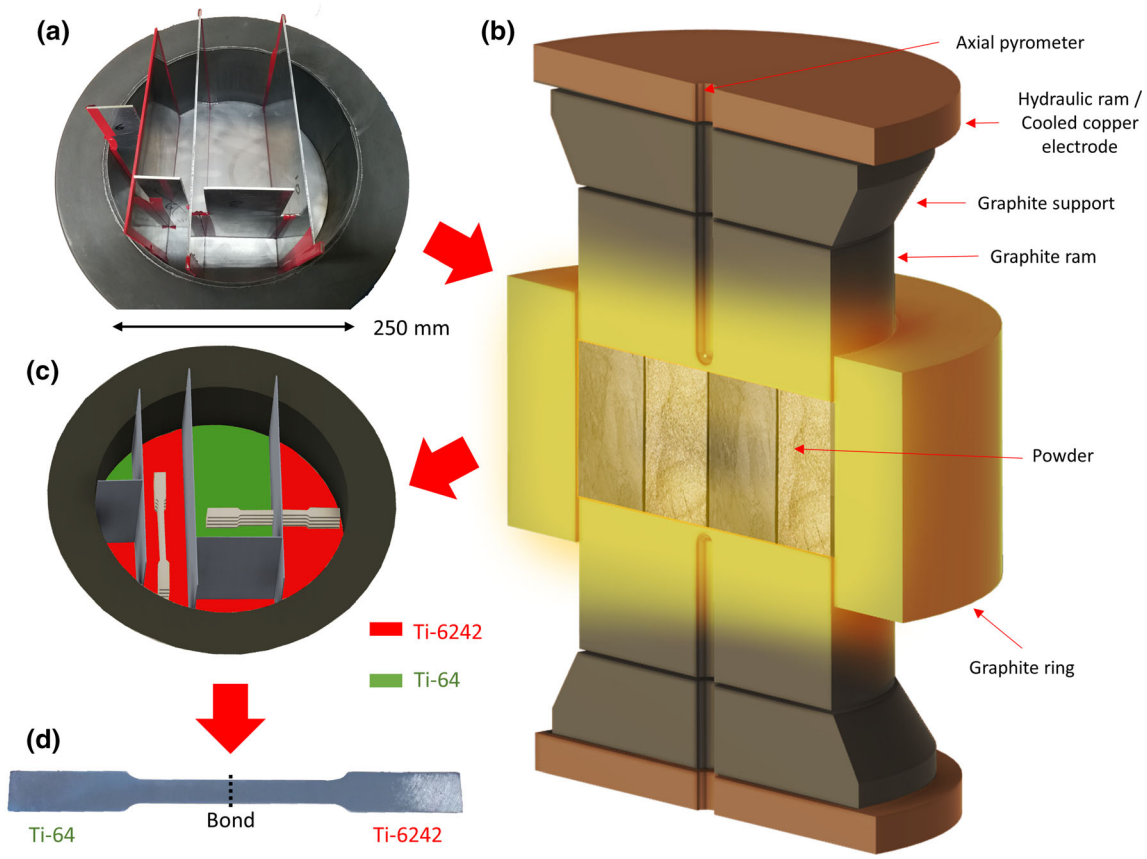

Fig. 3—A schematic illustration of the FAST-DB process used to manufacture the tensile test samples. (*a*) A photograph of the graphite ring with the aluminum dividers, (*b*) a schematic representation of graphite ring layout during the FAST process, (*c*) a schematic illustration of how the FAST-DB billet was machined, (*d*) a photograph of a 120 mm long FAST-DB tensile sample.

Correlate software to extract the strain data of the x and y plane and MATLAB to plot the data in a 2D graph. It was necessary to create a pattern in the surface of the sample to obtain good measurements with the DIC technique. First, the sample was sprayed with white paint to create a homogenous layer in the sample. Then, the sample was sprayed with black paint to create an irregular pattern in the surface which allowed the local deformation in the specimen to be constantly tracked using the GOM system.

D. *Optical Digital Image Correlation and Mechanical Loading*

Microscale *ex-situ* DIC was carried out after tensile loading using a Kammrath-Weiss 5kN tensile/compression microtester, under displacement control at a rate of 0.02 mm/min, equipped with a control unit to provide displacement and load data. Subsequently, the crosshead displacements were transformed to engineering strain by using the initial gauge length. All measurements in the strain maps are determined in the unloaded state, as the sample had to be removed from the microtester after each deformation stage. It was not possible to image the sample whilst positioned within the tester, due to being unable to move the sample to the correct height. Images were acquired using a Zeiss Axio Imager 2 optical microscope, equipped with built-in mapping software enabling many images to be captured without any significant reduction in image quality. Focus interpolation was used by placing 36 points across the surface that were manually focused and then used as reference points during the image capture. The images were taken at a resolution of 1648 x 1436 pixels^2 with a 20 pct overlap and at a spatial resolution of 0.547 μm/pixel. Each matrix of images were stitched together using ImageJ image processing software[50,51] prior to the DIC analysis. Loading and subsequent imaging was repeated up to low plastic strains. For the complete series of images, ImageJ was also used for image manipulation in terms of shift and rotation correction to enable easy correlation. The displacements were computed using LaVision's DIC software DaVis, version 8.4, using a standard fast Fourier transform (FFT) with an initial interrogation window size of 1024 x 1024 pixels^2 down to a final interrogation window size of 32 x 32 pixels^2 giving a spatial resolution of 17.51 x 17.51 μm^2. The strain analysis was performed using the in-house DefDAP 0.92 Python package,[52] where the microscale DIC is typically presented as effective shear strain, γ_{eff}, as this takes into account all of the in-plane components.[53,54] This was calculated by the standard relationship given in Eq. [1].

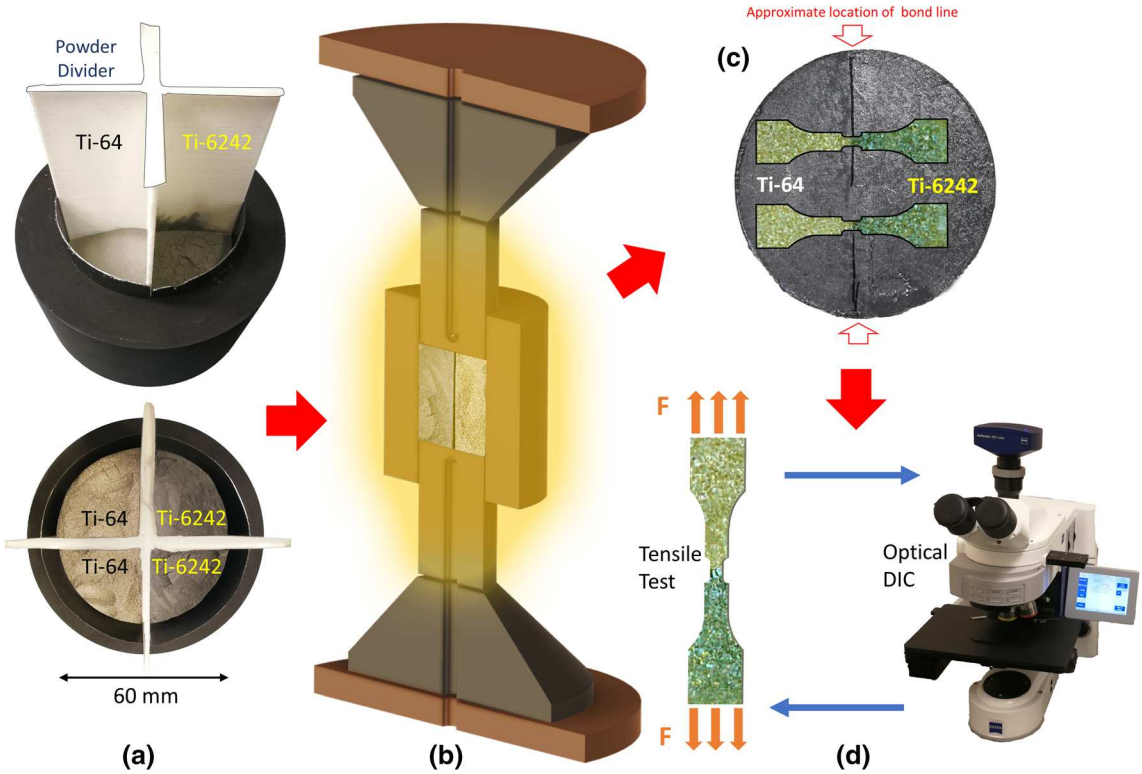

Fig. 4—A schematic illustration of the process used to test the bond with optical Digital Image Correlation (DIC). (*a*) photographs of the graphite ring die with the cross-shaped polymer divider arrangement, (*b*) a schematic representation of graphite ring layout during the FAST process, (*c*) an image showing a 50 mm long tensile sample superimposed onto a photograph of the FAST-DB billet and (*d*) a representation of the optical DIC procedure.

$$\gamma_{eff} = \sqrt{\left(\frac{(\varepsilon_{xx} - \varepsilon_{yy})}{2}\right)^2 + \left(\frac{(\varepsilon_{xy} + \varepsilon_{yx})}{2}\right)^2} \qquad [1]$$

where ε_{xx} is the strain in the loading direction, ε_{yy} is the strain normal to the loading direction and $\frac{(\varepsilon_{xy}+\varepsilon_{yx})}{2}$ is the in-plane shear component.

E. *Grain Texture Measurements Using Electron Backscatter Diffraction (EBSD)*

After mechanical loading, post-deformation EBSD was performed in the region of interest to enable the strain localization to be correlated to the underlying microstructure. Orientation mapping was performed in a Field Emission Gun (FEG) (FEI Sirion) Scanning Electron Microscope (SEM) equipped with an Aztec EBSD system and a Nordlys II detector, at an accelerating voltage of 20 kV. An area of 3 x 1 mm^2 was covered with a step size of 2.3 μm, to give sufficiently detailed grain orientation information for comparison with the 2D strain measurements.

F. *Analysis Techniques*

The tensile samples had to be sectioned before they could be metallographically prepared. A Struers Secotom-20 was used to section the materials. The specimens were then hot mounted with conductive Bakelite and ground with progressively finer grit SiC paper on a Struers Tegramin-25. A solution made of 0.06 μm colloidal silica with 10 pct of hydrogen peroxide was used to obtain a mirror finish in the surface of the specimen after the grinding stages. The micrographs were obtained with a FEI Inspect F50 SEM.

The local chemistry adjacent to the bond was measured with X-EDS point scans with a Philips XL30 SEM. The detector was calibrated with a pure cobalt standard at the beginning of each session. The chemical scanning was conducted perpendicular to the diffusion bond line, with a total of 15-20 points linearly spaced between them and a dwell time of 2 min per point. The data was plotted with the software MATLAB and the fitting curve were obtained with the curve fitting app in the same software using the complimentary error function given in Eq. [2].

The hardness profile of the material was measured with a Struers Durascan 70 G5. A total of 100 indentations, distributed in 5 rows, was perform across the bond. The 5 rows were parallel and diagonally crossed the bond in order to provide higher density of data points in the proximity of the bond, thus increasing the resolution of the hardness profile across bond. Each indentation had a dwell time of 15 s, in accordance with the ASTM E384 standard.[55] The load used for the indentation was 9.81 kgf for all the samples. The distance from each indentation to the bond was

measured manually with the software ImageJ from light micrographs and plotted with MATLAB.

III. RESULTS

A. *Tensile Behavior*

1. *Microstructure of FAST-DB consolidated preforms*

The microstructure obtained for the subtransus (TDB1) and the supertransus (TDB2) FAST-DB samples are shown in Figures 5(a) and (b). The primary observations are that (1) both conditions have achieved full consolidation and no porosity is evident and (2) processing in the subtransus region produces a much finer microstructure compared to when processing in the single-phase beta region (supertransus condition). In both cases the bond region thickness is of the order of 300 μm which agrees with the X-EDS measurements in Figure 6.

The subtransus microstructure consists of equiaxed primary alpha (~ 20 μm) which formed as recrystallized clusters at the original sites of particle-particle boundaries during processing. A more lath-type morphology evolves between these equiaxed alpha clusters, which is transformed secondary alpha from the beta that existed at 970 °C. This FAST microstructure is very similar to what would be observed in the as-HIP'ed condition.[56] This bimodal structure is far less apparent in the Ti-6242 compared to Ti-64: this is due to the finer Ti-6242 powder particle size which leads to a finer dispersion (and more homogeneous appearance) of equiaxed alpha, deriving from the particle-particle interfaces during consolidation. Although the secondary alpha laths are much less defined in Ti-6242 compared to Ti-64, there is a smooth chemical and microstructural transition across the bond. The only noticeable variation under backscattered electron imaging is the increase in Z contrast in both the alpha and residual beta phase of Ti-6242: this is due to the increased alloy additions with higher atomic weights, such as Zr and Sn in more creep resistant alloy.

The resultant microstructure in the supertransus FAST processed billet is a fully transformed large equiaxed grain structure with continuous grain boundary alpha due to the slow cooling (9 °C/min) after the 1030 °C and 1 hr dwell. The grain boundary alpha would have formed first during cooling and then the secondary alpha within the grains transformed from the beta phase. The grains in the mid-section of Figure 5(b) show evidence of chemical grading as the darker Ti-64 alpha laths morph into the brighter, more heavily stabilized Ti-6242 alpha without any noticeable change in secondary alpha size or morphology.

In the case of the supertransus condition, there is no noticeable change in grain size in the two alloys, and therefore the effects of the original powder sizes are nullified through the FAST processing after 1 hr dwell in

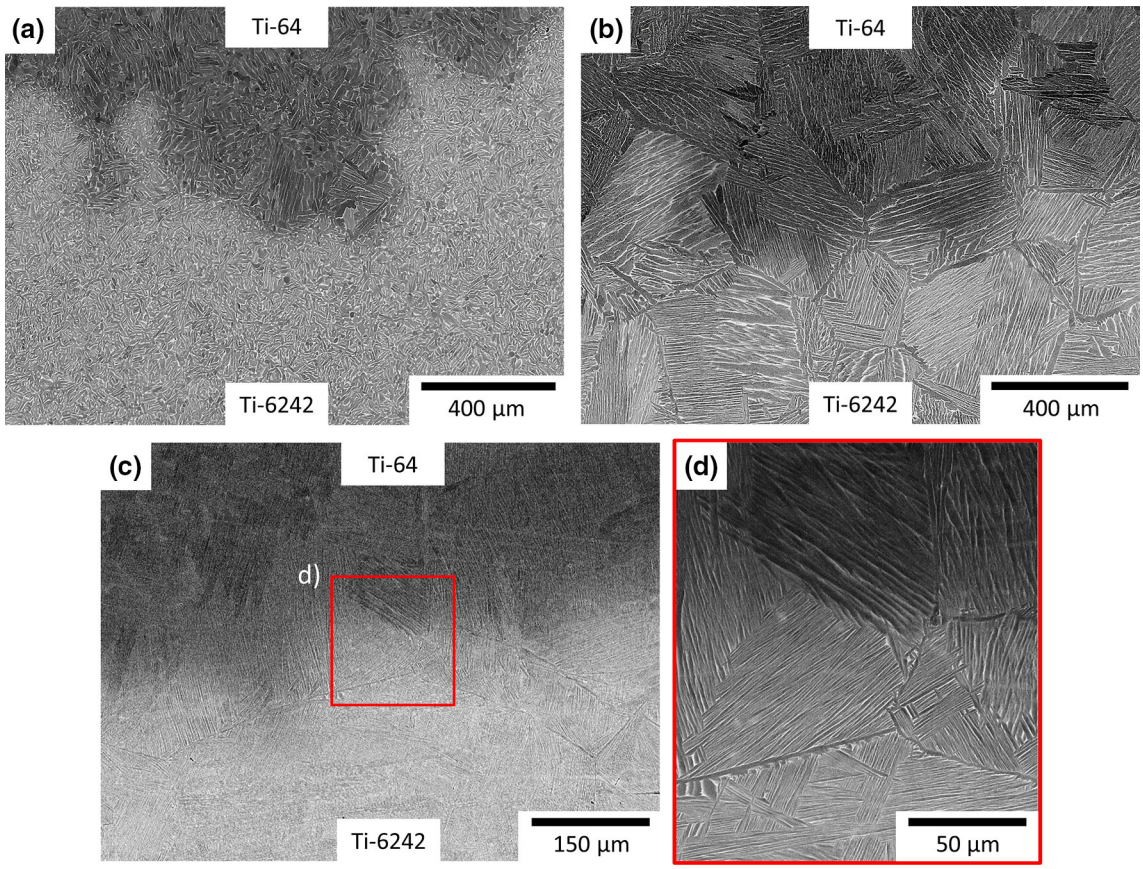

Fig. 5—Backscatter electron images of the FAST-DB sample processed under (*a*) subtransus conditions (TDB1), (*b*) supertransus conditions (TDB2), (*c*) supertransus conditions (TDIC), (*d*) supertransus conditions (TDIC) at higher magnification.

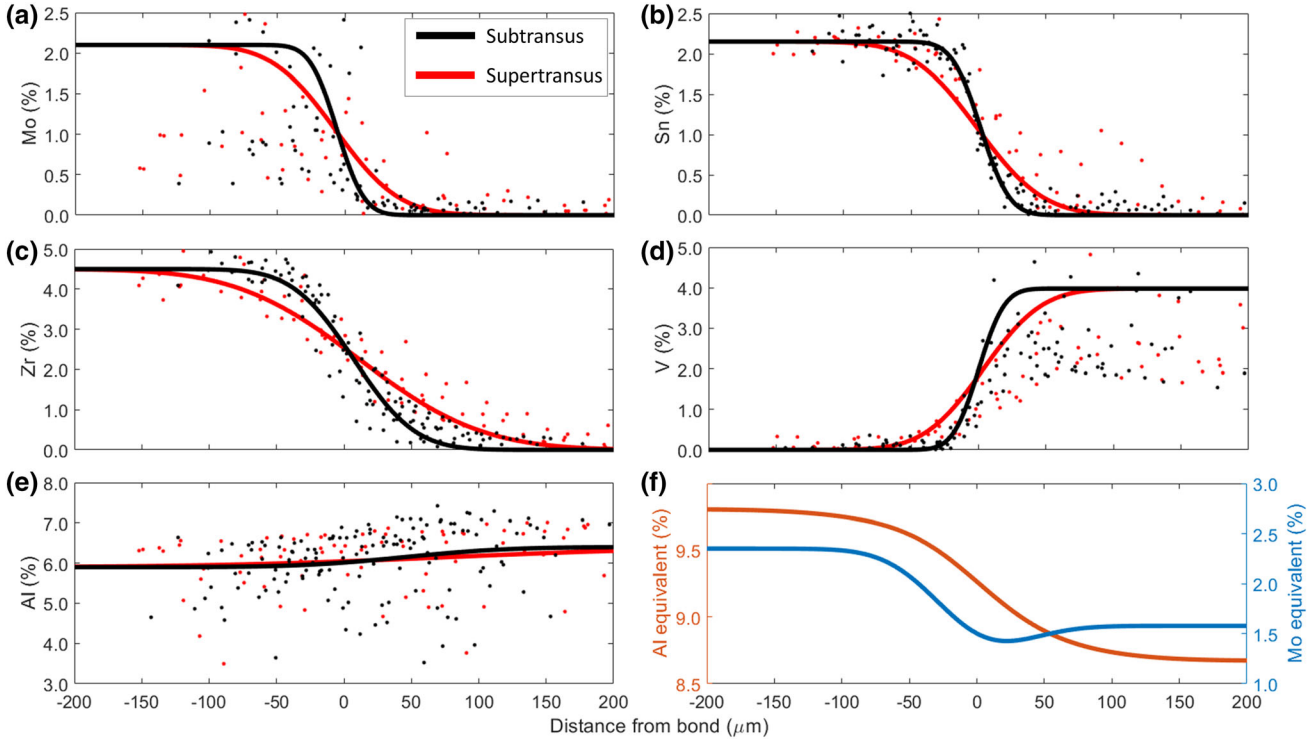

Fig. 6—Plots showing the element composition across a Ti-64 and a Ti-6242 bond when processed under subtransus and supertransus FAST conditions for: (*a*) Mo, (*b*) V, (*c*) Zr, (*d*) Sn and (*e*) Al. (*f*) Plot of the Al and Mo equivalent across the diffusion bond.

the single phase beta. This elimination of the effect of the original powder size is also observed with the TDIC sample in Figures 5(c) and (d), which used a smaller PSD powder than the powder used for TDB2, but obtained a similar grain size distribution.

The 60 mm diameter sample produced at the University of Sheffield had a higher cooling rate (63 °C/min) which resulted in a finer alpha lath colony size and more colony variant as shown in Figures 5(c) and (d). The powder was fully consolidated by achieving a density of 99.98 pct.

2. *Hardness and diffusion profile of the FAST-DB bond*

Figures 6(a) through (e) shows the gradual change of the elements across the diffusion bond in subtransus and supertransus processing conditions measured by X-EDS. It is important to measure the distance of the bond, as it will determine if the strain measured in certain areas is due to the diffusion bond or the base material. The variation of the chemical composition of the elements was curve fitted with the complimentary error function in Eq. [2].[24]

$$c = \frac{A_0}{2} erfc\left(\frac{x - J1}{2\sqrt{J2}}\right) \qquad [2]$$

C is the chemical composition of an element at a certain distance, A_0 is the initial element concentration, *erfc* is the complementary error function and x is the distance to the bond. The coefficients $J1$ and $J2$ were calculated by the curve fitting app in MATLAB to ensure the curves fit well with the data.

As expected, the diffusion gradient of the elements when FAST processed in the supertransus region is higher than when FAST processed under subtransus conditions. The variation between the supertransus and subtransus conditions tends to be around 100 μm. For supertransus processing conditions, the fastest interdiffusing element is Zr with a diffusion distance of 180 μm from the Ti-6242 into the Ti-64 alloy; the diffusion distances for Mo, Sn and V are very similar (~100 μm) at supertransus conditions. In the lower temperature, subtransus conditions, the diffusion distances are shorter, with Zr being the fastest diffuser at the bond interface. The maximum length of the diffusion bond in subtransus conditions is 150 μm, while for supertransus conditions the maximum distance is 350 μm. The diffusion profile of Al (Figure 6(e) is complicated to measure for both conditions because both titanium alloys have a very similar Al composition. Furthermore, the X-EDS measurements of Al have a high variation between them, which makes the curve fitting of the diffusion profile less accurate. Therefore, the diffusion of Al can be interpreted as constant through the diffusion bond.

Figure 6(f) shows the variation of Al and Mo equivalent across the diffusion bond for the supertransus conditions calculated with Eqs. [3] and [4].[57]

$$\text{Al eq (wt pct)} = \text{Al} + 10\,(\text{O} + \text{N} + \text{C}) + 1/3\text{Sn} + 1/6\text{Zr} \quad [3]$$

$$\text{Mo eq (wt pct)} = \text{Mo} + 2.5\text{Fe} + 2/3V + 1.25(\text{Cr} + \text{Ni} + \text{Cu}) + 1/3\text{Nb} \quad [4]$$

The curves show a higher value of Al and Mo equivalent for Ti-6242 than for Ti-64. The Al equivalent curve has a smooth transition between both alloys, but the Mo equivalent reaches the minimum value just after crossing the bond. This is because V is a faster diffuser in β-Ti compared to Mo. The data used to build these curves is based in the X-EDS data plotted in Figure 6(a) through (e). Therefore, it has to be taken into account that there are could be small variation to the actual Al and Mo equivalent.

The hardness of the bond is shown in Figure 7 for the subtransus and supertransus FAST processing conditions. The hardness has a similar value for both alloys and it does not show any variation when moving across the diffusion bond. There is scatter in the hardness data, especially for the TDB2, given that the hardness varies depending on the tested region and the grain orientation. On average, the hardness for the subtransus material is slightly higher than the supertransus material which is expected due to the finer grain structure (see Figure 5).

3. *Tensile behavior*

Tensile tests were carried out on the FAST-DB dissimilar alloy material (TDB1, TDB2) and the alloy Ti-6242 (T1, T2). As repeats for each condition were very consistent, Figure 8 displays one stress-strain plot for each material condition. Figure 8 shows the curves for the FAST-DB material (Ti-64/Ti6242) overlaid on the results for a sample made of one alloy (Ti-6242). The FAST-DB and Ti-6242 (monolithic) material have very similar yield characteristics in both subtransus and supertransus conditions: the only difference being that the FAST-DB material failed at a slightly lower strain with more localized deformation prior to failure compared to the equivalent Ti-6242 monolithic condition.

In both cases, when the specimen was processed under subtransus FAST conditions, a higher yield stress point and a higher ultimate tensile strength was obtained for both materials. Additionally, for the FAST-DB material, a decrease in the strain to failure was observed for TDB2 in relation to TDB1.

Overall, the values obtained in the tensile test are very similar to that obtained from material processed from the conventional processing route. However, it is also worth noting that the microstructure of the FAST-DB material has not been optimized to achieve the best results for a tensile test.

One sample of TDB1 and TDB2 was analyzed using DIC to characterize the strain localization during a tensile testing, for a FAST-DB sample when processed at sub- and supertransus temperatures. Figure 9(a) shows the local deformation of two specimens at a strain of 0.07 and it is apparent that the subtransus sample has three distinct regions with different levels of strain. The bulk Ti-6242 region accommodates the lowest strain, then there is a smooth transition of strain accumulation across the relatively small diffusion bond region into the bulk Ti-64 region - which accommodates the highest levels of strain. These three regions are clearly differentiated in the subtransus specimen.

In the supertransus FAST processed specimen, the grain size and transformed beta structure is very similar for both alloys, with large grains that cross the diffusion bond region (as shown in Figures 1 and 5). Due to the large grain structure these three regions are less distinct in the DIC strain map of the supertransus specimen and

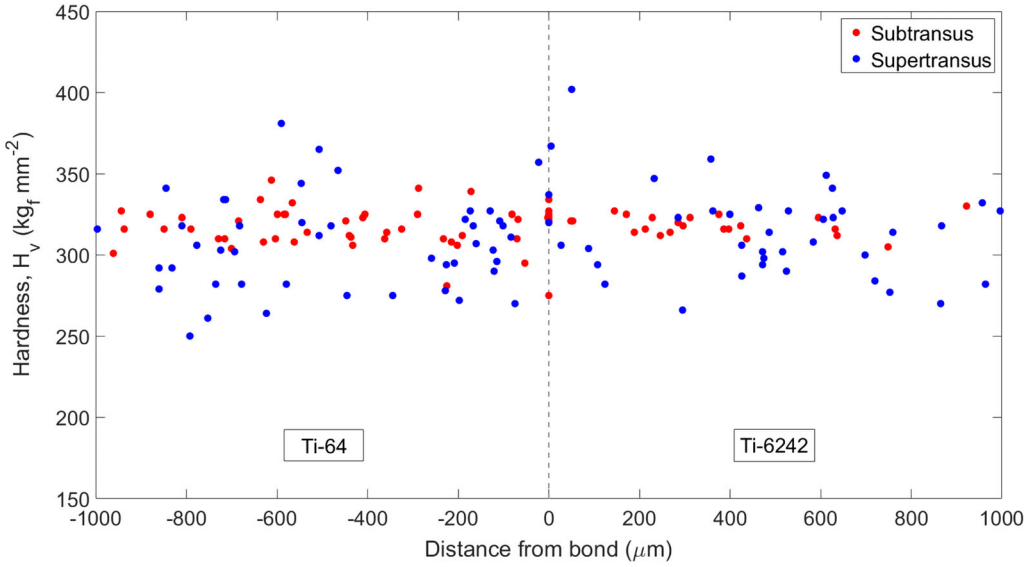

Fig. 7—Vickers microhardness profiles across the FAST-DB bonds processed under subtransus and supertransus conditions.

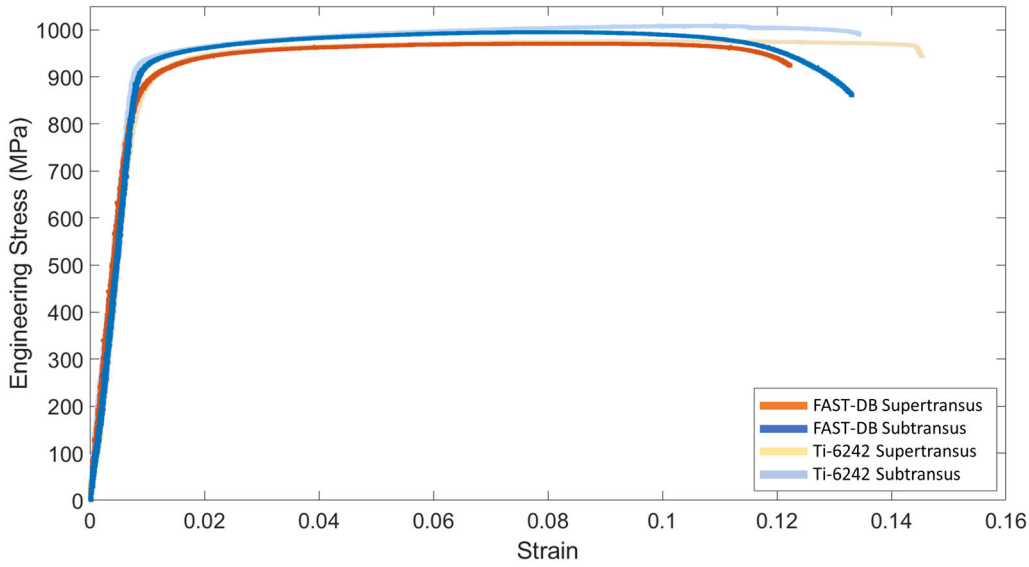

Fig. 8—Stress strain curves of ASTM E8/E8M specimens for the FAST-DB Ti-64/Ti-6242 dissimilar alloy material and Ti-6242 material, processed under subtransus and supertransus conditions.

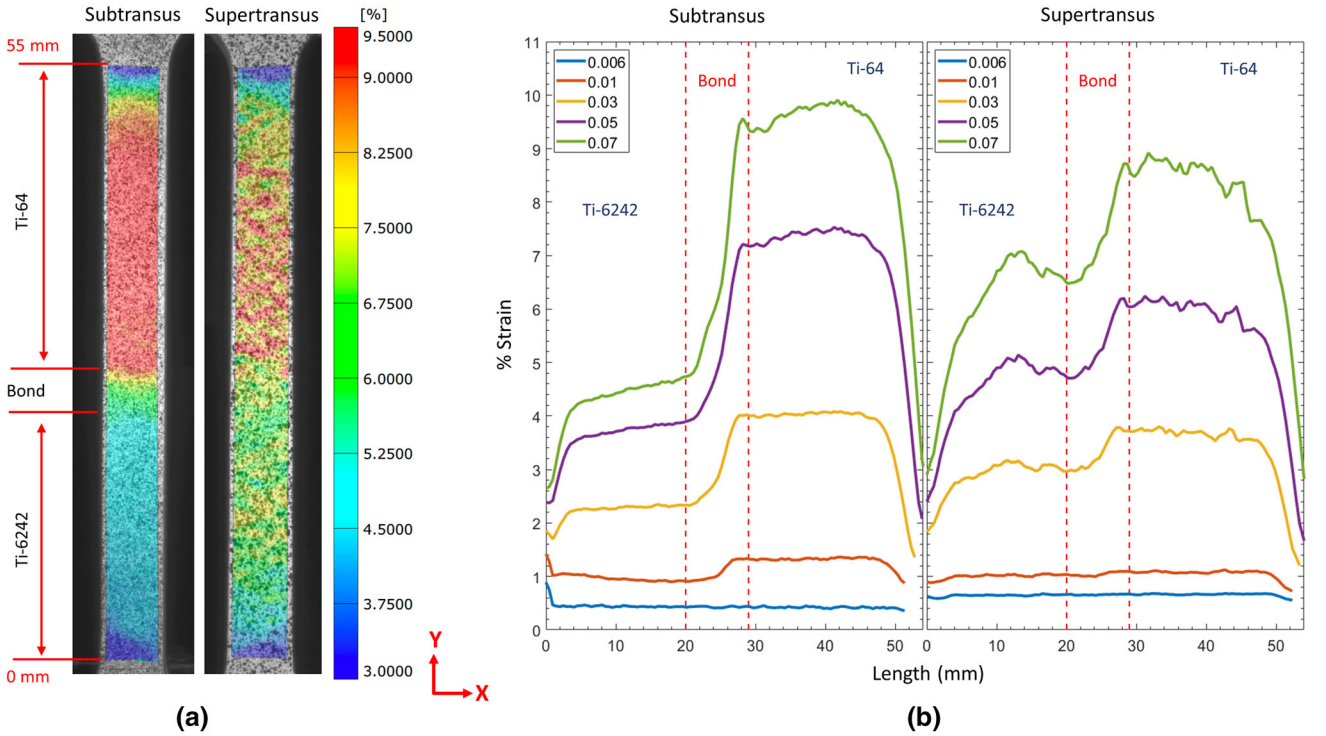

Fig. 9—Results obtained with the DIC performed to the standardize samples. An image of the strain in different parts of the sample is shown in (*a*) for a subtransus specimen and a supertransus specimen. (*b*) The two graphs show the average strain at each part of the subtransus and supertransus specimens at incremental stages of the tensile test.

the strain is distributed more homogeneously over the specimen.

In Figure 9(b) the average strain in the x direction is plotted against the y direction of the samples. From Figure 9(b), it is clear that for both processing conditions, the Ti-64 regions accommodate higher levels of strain than the Ti-6242 regions. Furthermore, in both cases, there is a smooth transition of strain across the diffusion bond from Ti-64 to Ti-6242. In the subtransus samples, the local difference in the strain between the two alloys is higher than the supertransus conditions as the strain is more homogenously distributed in the latter case. In fact, twice as much strain is accommodated in the Ti-64 region compared to the higher strength Ti-6242 alloy region when processed in the subtransus region.

All the FAST-DB samples fractured in the bulk Ti-64 region, which has a lower strength than alloy Ti-6242; as clearly shown in Figure 10(a). The two alloys for the subtransus material can be differentiated very well due to the surface cold deformation in Ti-64 at the high strain levels. For the supertransus material both alloys deformed in a similar manner (as observed in the DIC homogeneous strain profile in Figure 9(b)) and therefore it is more difficult to locate the bond line between the two alloys in Figure 10(b). From the data in Figure 9(b), the Ti-64 bulk material accommodated higher strains when FAST processed under subtransus conditions compared to the supertransus processed material. The subtransus failure is normal to the tensile axis, whereas the supertransus samples failed at a shear angle to the tensile axis, which indicates the fracture of the specimen is controlled by a combination of normal and shear stress failure.

The fracture surface of the subtransus specimens were much smoother compared to the supertransus specimens where rough-faceted fracture features were observed. Both types of materials suffered from a ductile fracture, as dimpled features were observed in the fractographs in Figure 10(c) through (f). The fracture surface for the subtransus processed material exhibited voids and an equiaxed dimple pattern that confirms a normal mode fracture. The supertransus processed material exhibited a transgranular failure due to the observation of cracks along the colonies of alpha laths. Additionally, parabolic shaped dimples were also observed indicating a shear mode stress component in the bottom region of the sample (Figure 10(f)).

B. *Optical Strain Map*

The deformation for the subtransus material was shown clearly in Figure 9 where there is a smooth transition across the bond. Nevertheless, the DIC technique used previously had insufficient spatial resolution to show the deformation for the supertransus material. Thus, mesoscale optical DIC technique was used during an interrupted tensile test of a FAST-DB specimen to characterize the evolution of local plastic strain across the bond - for a specimen processed under supertransus conditions. Although the higher resolution optical DIC is unable to resolve individual slip bands, it can detect local differences in strain between individual prior beta grains. The strain maps obtained from the optical DIC were complemented with EBSD orientation maps to calculate the α phase prismatic and basal Schmid factor. The calculation of the Schmid factor was done following the conventional approach where the global stress condition is used. With this approach, it is assumed that the nominal applied stress can be directly related to the stress state in the individual α grains.[40] This is a simplistic approach that ignores other factors but previous studies have found a strong agreement between the predicted Schmid factor and the actual active slip system in HCP metals.[58]

The specimens tested in Figure 9 have a similar diffusion and hardness profile as the material plotted in Figures 6 and 7 and the microstructures of such specimens are shown in Figures 5(c) and (d).

Figure 11(a) shows IPF maps of the diffusion bond between Ti-64 and Ti-6242. It can be observed that there is no clear indication that the two dissimilar alloys are joined from the crystal orientation map. There is no

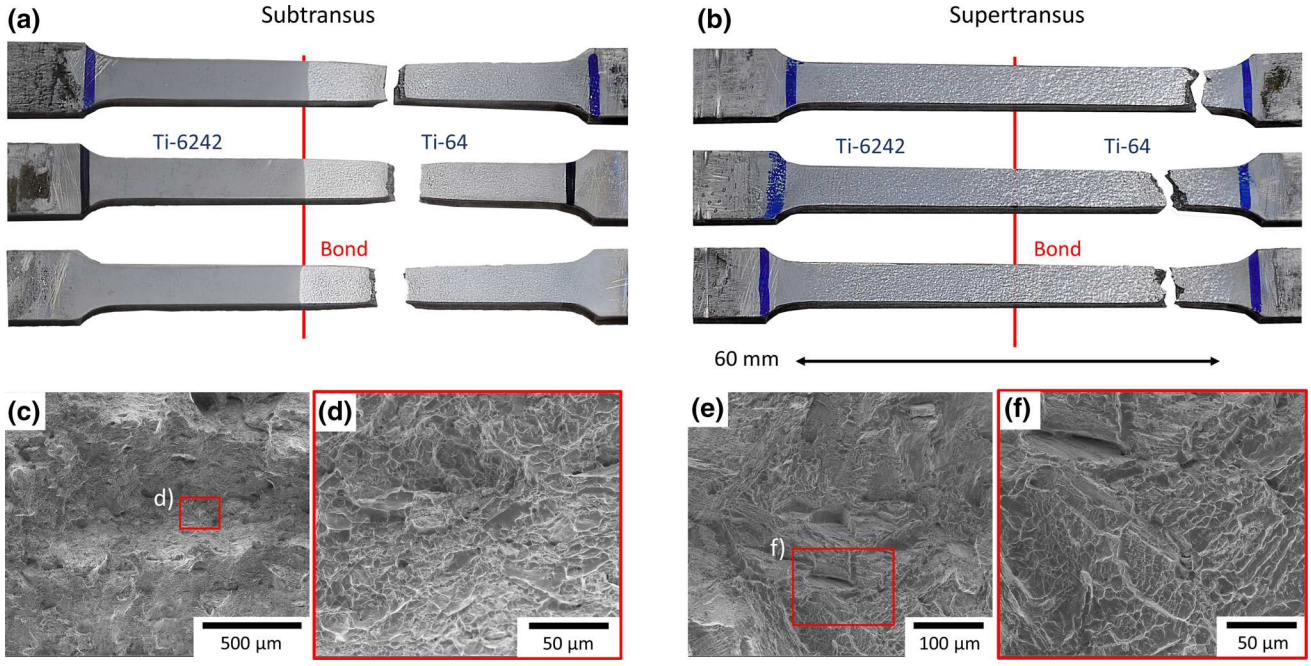

Fig. 10—Images of the failure location in the standard tensile test for the (*a*) subtransus specimens and (*b*) supertransus specimens. SEM fractographs of the fracture surface of the subtransus tensile specimens (*c*) at low and (*d*) high magnification, and for supertransus tensile specimens at (*e*) low and (*f*) high magnifications.

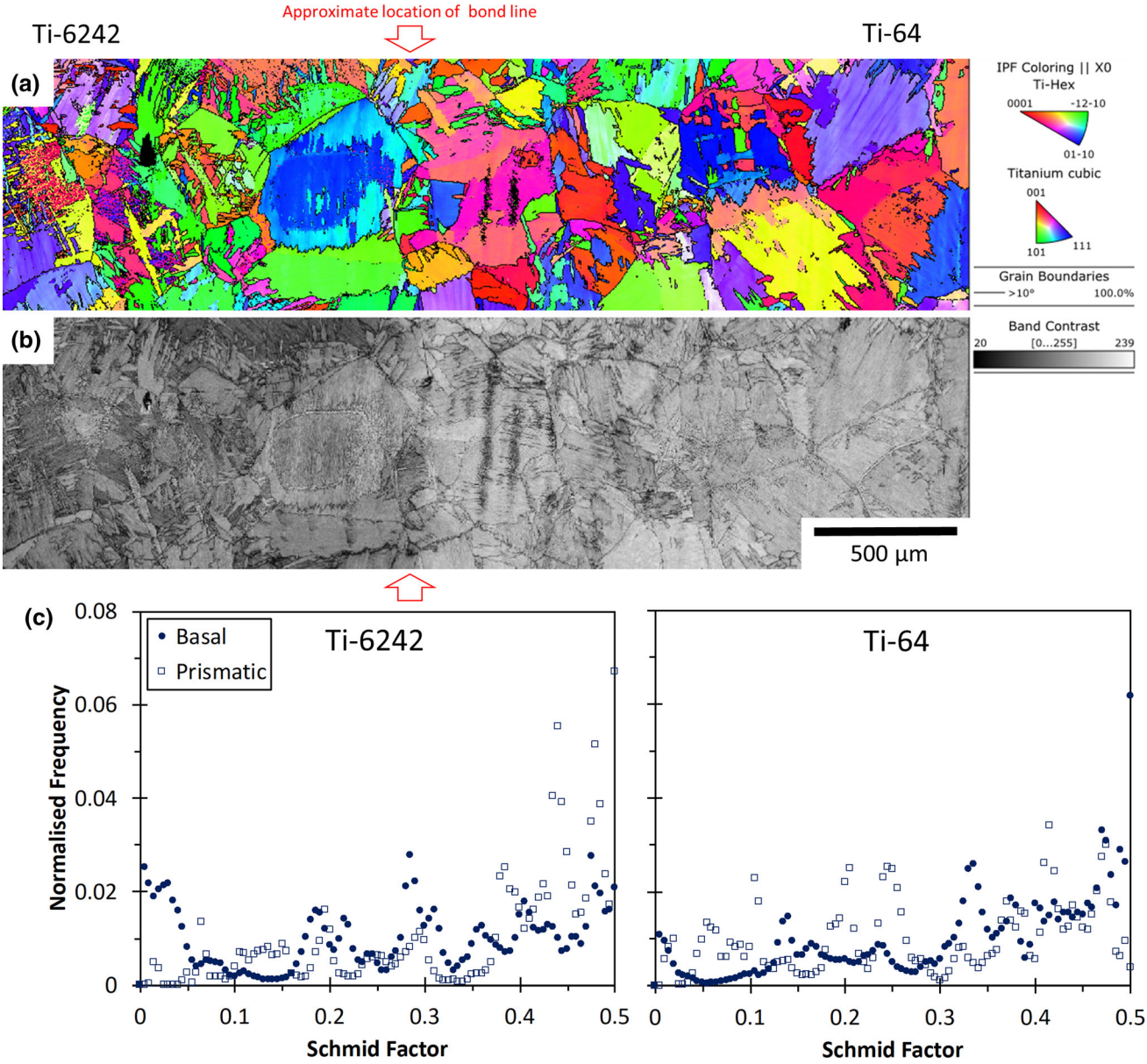

Fig. 11—(*a*) EBSD map of the FAST-DB bond with the IPF for titanium hexagonal and cubic. (*b*) Band contrast micrograph showing the location of the bond and the slip band located in the Ti-64 region. (*c*) Graphs plotting the normalized frequency against the Schmid Factor for the basal and prismatic plane in the Ti-6242 and the Ti-64 regions.

clear mismatch between the two alloys, and some grains contain a chemical grading from Ti-64 to Ti-6242 across the diffusion bond. However, from the band contrast map in Figure 11(b), the location of the bond can be roughly estimated due to the gradual change in contrast from one region to the other, where the Ti-6242 side is slightly darker than the right, Ti-64 side. For a more quantitative comparison of the orientations of the grains for each alloy, normalized frequency distributions of the Schmid factor have been plotted in Figure 11(c), for both basal and prismatic slip in each side of the bond, where the Schmid factor provides an assessment of the relative ease of slip. The results show that the highest Schmid factor frequency in the specimen is in the Ti-6242 side for the values between 0.4 and 0.5 in the prismatic plane. The Schmid factor for Ti-64 is similar for the basal and prismatic planes and the frequency shows a small increase for values between 0.4 and 0.5. Furthermore, the prediction of plastic strain in the two alloys was based purely on the Schmid factor information, it would be expected to see more concentrated deformation in Ti-6242 due to the higher number of grains with Schmid factor values of 0.4 and above.[40]

The Schmid factor maps for the prismatic and basal planes across the FAST-DB bond are plotted in Figures 12(a) and (b). Figure 12(c) shows a micrograph of the etched microstructure of the tensile specimen in the diffusion bond region. This micrograph can be correlated with the optical effective shear strain map shown in Figure 12(d). It has to be taken into account

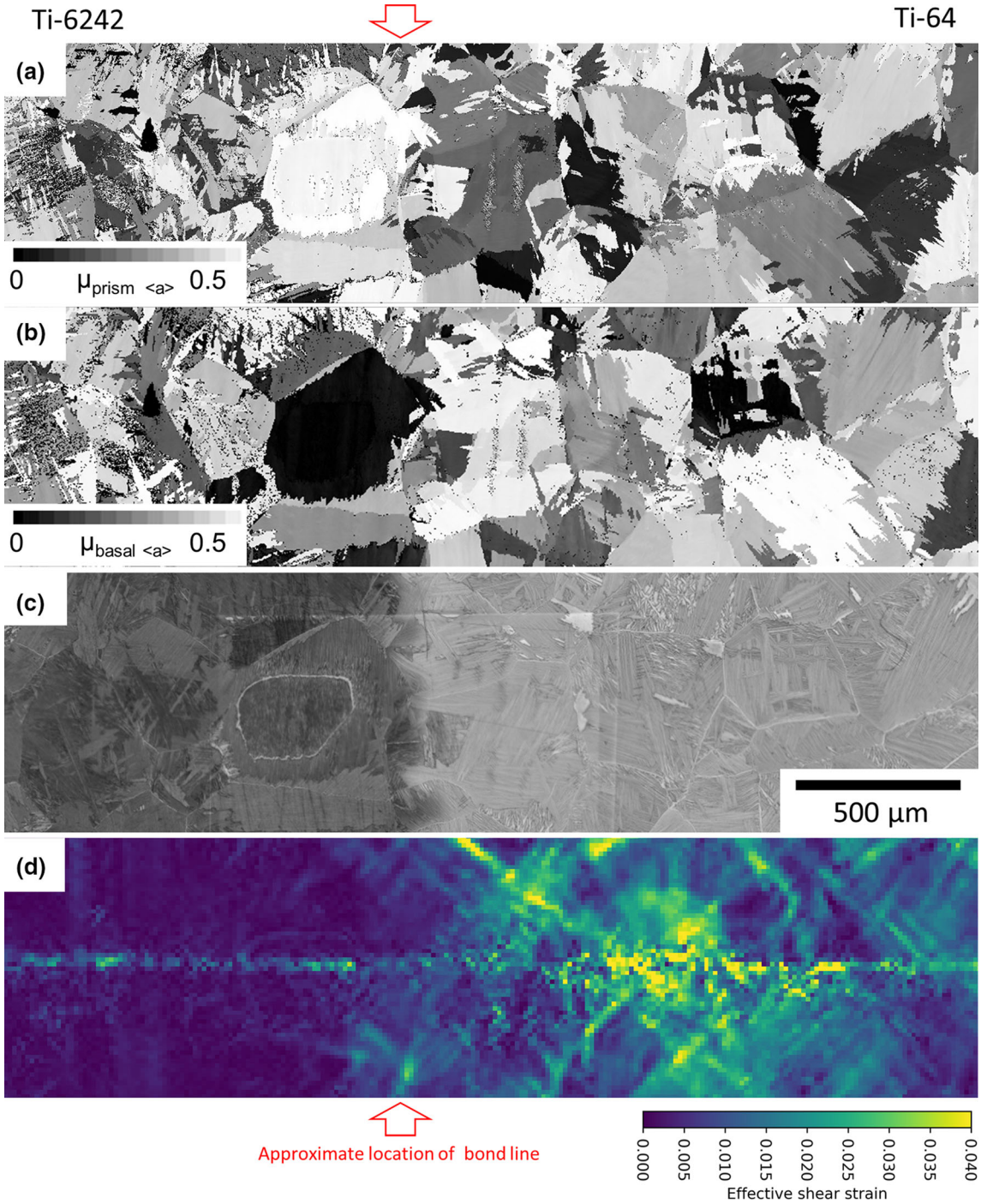

Fig. 12—Mapping of the Schmid factor for the (*a*) prismatic and (*b*) basal planes. (*c*) Optical micrograph of the FAST-DB bond after etching with HF. (*d*) Mapping of the effective shear stresses in the FAST-DB sample after applying tensile strength.

that Figure 12(d) has a horizontal line going across the specimen that does not represent the real strain value. These artefacts are a result of slight misalignments between individual frames that cannot be corrected during the stitching process, but they do not mask the underlying deformation of the material. It is clear that all the deformation has occurred in the Ti-64 region with just a little deformation happening on the diffusion bond on the bottom of the sample.

This is evident in Figure 13 where the effective shear strain for all the specimen is mapped and plotted. It should be noted that the two horizonal lines showing strain across the samples in Figure 13(a) are the same stitching artefacts as observed in Figure 12(d). The plot in Figure 13(b) and (c) show the average shear strain and the 95th percentile values are plotted against the distance, in a similar way to Figure 9(b). These values were calculated from each vertical column of pixel data

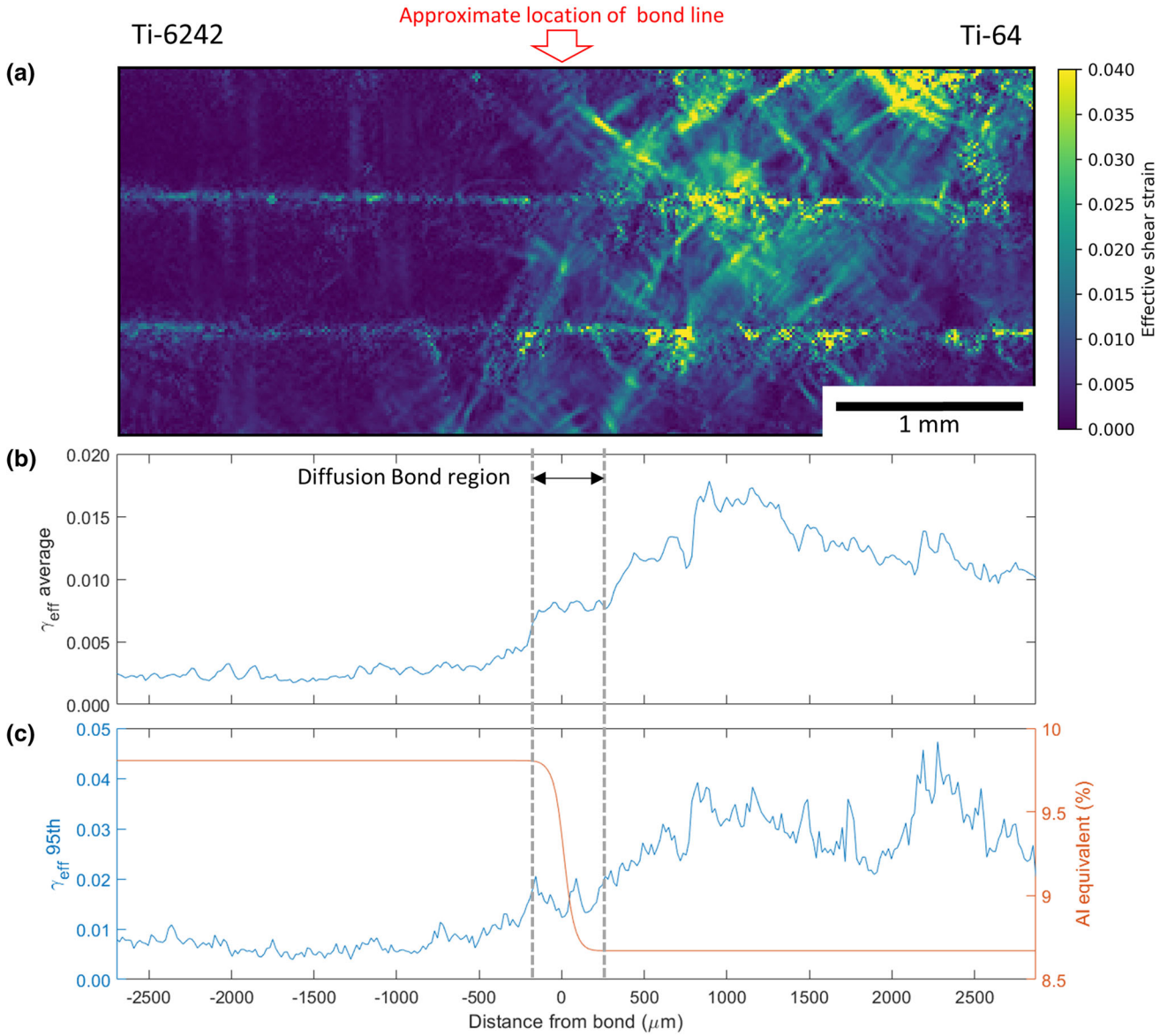

Fig. 13—(*a*) Mapping of the effective shear stresses in the FAST-DB specimen after applying tensile strength. Development of the effective shear strain profiles across the FAST-DB bond for (*b*) the average effective shear strain and (*c*) the 95th percentile of effective shear strain.

in the width direction of the sample. The 95th percentile value is used to highlight the comparative maximum level of strain in each column. Additionally, the 95th percentile value was used instead of the maximum value to avoid excessive noise from the data.

The graph in Figure 13(b) shows three defined regions. First, the strain is constant in Ti-6242 until a sharp increase of strain occurs at the start of the diffusion zone. Then, the strain remains constant across the diffusion bond region and increases when the composition is entirely Ti-64, which correlates with the observations in the standard tensile test. Furthermore, there are two main peaks in the Ti-64 region and the closest one to the bond is located at around 800 μm. The maximum effective shear strain between the two alloys is about four times higher in Ti-64 compared to Ti-6242. For the chemically graded, diffusion bond region, the maximum effective shear strain is approximately three times lower than the bulk Ti-64 and approximately two times higher than that measured in the Ti-6242 bulk. Lunt *et al.*[47,48] observed similar levels of maximum shear strain in the grain boundaries of a Ti-64 produced by plasma wire deposition.

IV. DISCUSSION

A. *Bond Characterization*

The results presented in Figure 6 show a higher diffusion of elements for the samples processed at supertransus temperatures compared to those at sub-transus conditions. There are two main reasons for this difference; first, the diffusion coefficients follow an Arrhenius law, that increases as temperature

increases.[12,59] Secondly, titanium is an allotropic material with a dominant HCP crystal structure when processing below the beta transus and a BCC crystal structure above the beta transus. It has been proven that the BCC beta phase has three orders of magnitude greater diffusion than the HCP alpha phase, which correlates well with the results obtained in this study. Furthermore, the diffusion in the HCP alpha phase is anisotropic and is dependent on the orientation of the c-axis.[60]

The change in diffusion kinetics when the sample is processed above and below the beta transus has no effect on the average hardness value across the bond, as shown in Figure 7. Nevertheless, it is possible to appreciate that throughout the sample, the supertransus hardness measurements are more scattered compared to the subtransus condition. This variation is due to the different microstructures developed after FAST processing (Figure 5). The supertransus processed microstructure consists of large grains while the subtransus samples consists of much finer grains. Hence, in the case of the supertransus sample, the hardness indenter tends to apply the load in one large grain, whereas in the subtransus sample, multiple finer grains are tested. The HCP crystal structure has different hardness values depending on the orientation tested.[61] Therefore, testing individual grains - as in the supertransus condition - results in higher variability in the hardness measurements than the average hardness value generated from testing multiple grains – in the subtransus condition. Furthermore, the hardness of the alpha and beta phases are different and the hardness measurements depend on the volume fraction of each phase.[62] Consequently, for the supertransus microstructure, the volume fraction of alpha and beta measured will vary depending if the measurement is taken at the center of the grain or at the alpha-rich grain boundary. Meanwhile, the amount of alpha and beta phase tested for the subtransus material is more homogenous due to the finer microstructure distributed throughout the sample.

B. *Deformation Behavior of the Bond*

The use of DIC provides a more in-depth understanding of the deformation behavior of FAST-DB material processed at sub- and supertransus temperatures, as shown in Figure 9(a). However, the technique has some limitations in terms of resolution because it calculates the strain of a region by averaging several pixels together. Thus, the subtransus specimen shows three well defined strain regions, as the fine grained microstructure for the subtransus specimen results in the DIC averaging multiple grains. The supertransus specimen shows a graded, less defined variation of strain across the specimen as the DIC is averaging a smaller number of grains due to the larger grain size.

The dissimilar deformation observed in Figure 9 is due to the differences in mechanical properties between the two alloys: Ti-6242 has a yield strength ~70MPa higher than Ti-64, hence, the Ti-64 region plastically deforms before the Ti-6242 region. This is shown very clearly in Figure 9(b), where after a total strain of 0.01, the degree of plastic deformation partitioned in the Ti-64 region is much higher than in the Ti-6242.

Another observation is that the microstructural condition of these FAST-DB samples impacts on the differential strain observed between Ti-64 and Ti-6242 regions when processed at sub- and supertransus temperatures. As shown in Figure 5(a), the Ti-6242 region in the subtransus specimen has a finer microstructure than the Ti-64 region, leading to higher tensile properties due to the shorter slip length. Meanwhile, the supertransus sample has a very similar microstructure in both alloys, for this reason the difference in strain between the two alloys in this sample is dominated by the differential alloy chemistry. The finer Ti-6242 microstructure in the subtransus FAST-DB sample (leading to defined strain regions in the DIC analysis) explains the higher ductility to failure compared to the supertransus specimen in Figure 8, even though the strain was distributed more homogeneously in the latter. Furthermore, it is shown in Figure 9(b) that Ti-64 subtransus can withstand more plastic deformation than the supertransus microstructure, which is demonstrated by the stress strain curves (Figure 8) and the fracture location in Figure 10.

The use of optical DIC has provided a better understanding of the local deformation across the chemically graded diffusion bond for supertransus specimens. In Figure 12, the results in the Ti-64 region are similar to the ones observed by Littlewood *et al.*[46] for forged Ti-64, in which grains with higher Schmid factor had 3 times more strain than grains with lower Schmid factors. From Figure 12(a), it was expected to see some strain in the soft grain next to the bond because it had a high Schmid factor: the same grain is a hard oriented grain in the basal plane, but it has been reported that slip in prismatic plane has lower CRSS than the basal plane.[3,27,33,34] However, there is no effective shear strain in that region. For the basal plane, there is a soft grain next to the bond but again, very little strain is observed in that region. Figure 12(d) has a similar evolution of the strain than the subtransus specimen observed in Figure 9(a). In both figures, there is high strain in the Ti-64 region, then, there is a decrease of strain in the bond and it finishes with very low strain in Ti-6242.

The transition region measured in the optical DIC test is more accurate than the one calculated from the standard tensile test (Figure 9(b)): this region has been highlighted with grey dotted lines in Figure 13(b) and (c) and it shows a region with a constant value of effective shear strain. The distance of that region is approximately 410 μm and the total diffusion length for Zr in the bond is around 360 μm as shown in Figure 6(b). Although the region in Figures 13(b) and (c) is larger than the measured diffusion in Figure 6(b), it has to be taken into account that this measurement was taken after applying strain to the specimen. Therefore, it is possible that the diffusion distance across the bond is slightly greater than the original measurement. It is clear that the bond acts as a transition zone between the two alloys and that high shear strains and deformation will partition to the lowest strength alloy, i.e. – Ti-64:

interestingly, even when a soft oriented grain for easy prismatic slip is present in the bond.

The distinct change in shear stress across the bond correlates with the chemical grading and variation in Al and Mo equivalents from Ti-64 to Ti-6242 as shown in Figure 13(c) for Al equivalent. The Al and Mo equivalent are calculated from Eqs. [3] and [4] and the information in Table II.

For Ti-6242, the Al equivalent is 9.44 pct and the Mo equivalent is 2.05 pct; for Ti-64, the Al equivalent is 8.09 pct and the Mo equivalent is 2.84 pct. There is a difference of 1.35 pct in the Al equivalent and 0.79 pct in the Mo equivalent between the alloys. In the bond region, the Al equivalent is always higher than in the bulk Ti-64, as shown in Figure 6(f). Previous studies[63,64] observed an increment in the strength of the alloy with the increase of the Al or Mo equivalent in titanium alloys. The results also showed that the effect of Al equivalent was more significant than Mo equivalent in the strength of the alloy. Additionally, Williams *et al.*[33] observed that the CRSS increased in a TiAl alloy when the Al content increased. This could explain the fact that there is no effective shear in the soft grain for the prismatic plane that is crossing the bond in Figure 12.

The higher Al equivalent content will increase the strength of the alloy due to a higher solid solution strengthening effect.[57] This agrees with the observed deformation within the diffusion bond when there is gradual change in the alloy chemistry from Ti-64 to Ti-6242. The Al equivalent profile across the diffusion bond, shown in Figure 13(c), has a smooth transition between the alloys and it reaches its lowest value in the bulk Ti-64. Therefore, the diffusion bond region has a local higher strength due to the higher solid solution strengthening effect compared to the bulk Ti-64. However, it is important to consider that the microstructural variables can affect the performance of the bond and not all titanium alloy combinations have a smooth transition across the bond. For example, Pope *et al.*[24] observed a fine secondary alpha in the diffusion bond region between Ti-5553 with CP-Ti or Ti-64, which created a hardness peak at the bond. The tensile samples still failed in the lower strength alloy, but the unexpected microstructure in the bond could have reduced the mechanical integrity of the bond.

V. CONCLUSIONS

The tensile deformation behavior of a diffusion bond between Ti-64 and Ti-6242 powders produced using FAST has been investigated using DIC at the macroscale and mesoscale. The results obtained with the optical DIC have been correlated with EBSD maps and the Schmid factor in the basal and prismatic system.

- FAST has successfully diffusion bonded the titanium alloys powders Ti-64 and Ti-6242 into a fully consolidated solid component with porosity levels below 0.01 pct. There is a smooth transition of the microstructure across the diffusion bond. The thickness of the bond is less than 300 μm and the hardness was constant across the bond.
- The standard tensile test showed that the failure occurred in the lower strength alloy - Ti-64. The samples processed under subtransus conditions had a smooth transition of the strain across the bond with low strain in Ti-6242 and high strain in Ti-64. The samples processed under supertransus conditions had a more homogenous strain across the sample, but there was still a visible transition of the strain between the alloys. The values obtained for the standard tensile test are similar to the values expected for titanium samples processed through the conventional processing and the failure occurred in the Ti-64 region.
- The EBSD maps of the FAST-DB bonds showed that there is no strong crystallographic texture in the FAST material. Furthermore, it is not possible to determine the exact location of the bond just from the IPF orientation map, it is necessary to use a band contrast map or use backscattered imaging in the SEM.
- It has been possible to observe deformation of the FAST-DB tensile test at a mesoscale level using optical DIC. As expected, most of the strain partitioned in the Ti-64 grains with reduced deformation occurring in the bond and very minimal slip localization in higher strength Ti-6242 alloy. The results also showed that a grain in the bond that has a similar or even more favorable orientation for the prismatic slip than a grain in the Ti-64 region shows little deformation yet the grain in Ti-64 deforms.
- The local higher strength of the bond region in comparison to the Ti-64 bulk is due to the solid solution strengthening effect in the diffusion bond compared to Ti-64.

ACKNOWLEDGMENTS

The primary author acknowledges the support of industrial sponsor, Rolls-Royce plc, and EPSRC grant EP/L016273 Centre for Doctoral Training in Advanced Metallic Systems for supporting this research. The provision of materials and supporting information from Rolls-Royce plc. is gratefully acknowledged. The authors also acknowledge the valuable contribution of Jacob Pope and Christopher Todd for technical assistance and Nicholas Weston and Adam Tudball for FAST technical support.

OPEN ACCESS

This article is licensed under a Creative Commons Attribution 4.0 International License, which permits use, sharing, adaptation, distribution and reproduction in any medium or format, as long as you give

appropriate credit to the original author(s) and the source, provide a link to the Creative Commons licence, and indicate if changes were made. The images or other third party material in this article are included in the article's Creative Commons licence, unless indicated otherwise in a credit line to the material. If material is not included in the article's Creative Commons licence and your intended use is not permitted by statutory regulation or exceeds the permitted use, you will need to obtain permission directly from the copyright holder. To view a copy of this licence, visit http://creativecommons.org/licenses/by/4.0/.

REFERENCES

1. V.A. Joshi: *An Atlas of Structures and Fracture Features*, 1st ed., CRC Press, Boca Raton, FL, 2006, pp. 7–15.
2. A.P. Mouritz: *Introduction to Aerospace Materials*, 1st ed., Woodhead, Cambridge, UK, 2012, pp. 15–38.
3. G. Lutjering and J.C. Williams: *Titanium*, 2nd ed., Springer, New York, 2007, pp. 15–50.
4. C. Leyens and M. Peters: *Titanium and Titanium Alloys*, 1st ed., Weinheim, DE, Wiley-Vch, 2003, pp. 1–36.
5. S. Babu, W. Peter, R. Dehoff, and L.J. Love, Report on Additive Manufacturing for Large-Scale Metals Workshop. (Oak Ridge National Laboratory, 2016) https://info.ornl.gov/sites/publications/files/Pub62831.pdf. Accessed 19 Nov 2020.
6. M. Suárez, A. Fernández, J.L. Menéndez, R. Torrecillas, H.U. Kessel, J. Hennicke, R. Kirchner, and T. Kessel: *Sintering Applications*, 1st ed., London, UK, IntechOpen, 2013, pp. 319–42.
7. O. Guillon, J. Gonzalez-Julian, B. Dargatz, T. Kessel, G. Schierning, J. Räthel, and M. Herrmann: *Adv. Eng. Mater.*, 2014, vol. 16 (7), pp. 830–49.
8. Z.Y. Hu, Z.H. Zhang, X.W. Cheng, F.C. Wang, Y.F. Zhang, and S.L. Li: *Mater. Des.*, 2020, vol. 191, p. 108662.
9. N.S. Weston, B. Thomas, and M. Jackson: *Mater. Sci. Technol.*, 2019, vol. 35 (11), pp. 1306–28.
10. S. Deng, R. Li, T. Yuan, P. Cao, and S. Xie: *Metall. Mater. Trans. A*, 2019, vol. 50A (6), pp. 2886–97.
11. Z. Trzaska, R. Cours, and J. Monchoux: *Metall. Mater. Trans. A*, 2018, vol. 49A (10), pp. 4849–59.
12. R. Li, T. Yuan, X. Liu, and K. Zhou: *Scr. Mater.*, 2016, vol. 110, pp. 105–08.
13. R. Li, P. Niu, S. Deng, T. Yuan, and G. Liu: *Metall. Mater. Trans. B*, 2020, vol. 51B (1), pp. 6–10.
14. J.P. Kelly and O.A. Graeve: *JOM*, 2015, vol. 67 (1), pp. 29–33.
15. C. Manière, L. Durand, A. Weibel, G. Chevallier, and C. Estournès: *Scr. Mater.*, 2016, vol. 124, pp. 126–28.
16. C. Manière, E. Torresani, and E.A. Olevsky: *Materials*, 2019, vol. 12 (4), p. 557.
17. C. Manière, E. Nigito, L. Durand, A. Weibel, Y. Beynet, and C. Estournès: *Powder Technol.*, 2017, vol. 320, pp. 340–45.
18. T. Voisin, J.-P. Monchoux, L. Durand, N. Karnatak, M. Thomas, and A. Couret: *Adv. Eng. Mater.*, 2015, vol. 17 (10), pp. 1408–13.
19. N.S. Weston and M. Jackson: *J. Mater. Process. Technol.*, 2017, vol. 243, pp. 335–46.
20. E. Calvert, B. Wynne, N. Weston, A. Tudball, and M. Jackson: *J. Mater. Process. Technol.*, 2018, vol. 254, pp. 158–70.
21. J. Pope and M. Jackson: *Metals*, 2019, vol. 9 (6), p. 654.
22. O. Levano, N. Weston, J. Pope, A. Tudball, D. Lunn, G. Baxter, and M. Jackson: *MATEC Web Conf.*, 2020, vol. 321, p. 03010.
23. N.S. Weston and M. Jackson: *Metals*, 2020, vol. 10 (2), p. 296.
24. J.J. Pope, E.L. Calvert, N.S. Weston, and M. Jackson: *J. Mater. Process. Technol.*, 2019, vol. 269, pp. 200–207.
25. D. He, Z. Fu, W. Wang, J. Zhang, Z.A. Munir, and P. Liu: *Mater. Sci. Eng., A*, 2012, vol. 535, pp. 182–88.
26. A. Miriyev, A. Stern, E. Tuval, S. Kalabukhov, Z. Hooper, and N. Frage: *J. Mater. Process. Technol.*, 2013, vol. 213 (2), pp. 161–66.
27. N. NaveenKumar, G.D. JanakiRam, S.S. Bhattacharya, H.C. Dey, and S.K. Albert: *Trans. Indian Inst. Met.*, 2015, vol. 213 (2), pp. 287–97.
28. P. Pripanapong, S. Kariya, T. Luangvaranunt, J. Umeda, S. Tsutsumi, M. Takahashi, and K. Kondoh: *Materials*, 2016, vol. 9 (8), p. 665.
29. P. Pripanapong, J. Umeda, H. Imai, M. Takahashi, and K. Kondoh: *Int. J. Eng. Innov. Res.*, 2016, vol. 5 (4), pp. 253–59.
30. K. Zhao, Y. Liu, L. Huang, B. Liu, and Y. He: *J. Mater. Process. Technol.*, 2016, vol. 230, pp. 272–79.
31. N. Vicente, A. Fedrizzi, N. Bazzanella, F. Casari, F. Buccioti, and A. Molinari: *Powder Metall.*, 2013, vol. 56 (2), pp. 143–48.
32. G. Martin, D. Fabrègue, F. Mercier, J.A. Chafino-Aixa, R. Dendievel, and J.J. Blandin: *Scr. Mater.*, 2016, vol. 122, pp. 5–9.
33. J.C. Williams, R.G. Baggerly, and N.E. Paton: *Metall. Mater. Trans. A*, 2002, vol. 33A (3), pp. 837–50.
34. H. Numakura, Y. Minonishi, and M. Koiwa: *Scr. Metall.*, 1986, vol. 20 (11), pp. 1581–86.
35. Y. Minonishi, S. Morozumi, and H. Yoshinaga: *Scr. Metall.*, 1982, vol. 16 (4), pp. 427–30.
36. I. Bantounas, D. Dye, and T.C. Lindley: *Acta Mater.*, 2009, vol. 57 (12), pp. 3584–95.
37. W.B. Hutchinson and M.R. Barnett: *Scr. Mater.*, 2010, vol. 63 (7), pp. 737–40.
38. S. Zaefferer: *Mater. Sci. Eng., A*, 2003, vol. 344 (1–2), pp. 20–30.
39. I.P. Jones and W.B. Hutchinson: *Acta Metall.*, 1981, vol. 63 (6), pp. 951–68.
40. F. Bridier, P. Villechaise, and J. Mendez: *Acta Mater.*, 2005, vol. 53 (3), pp. 555–67.
41. D. Lunt, T. Busolo, X. Xu, J. Quinta da Fonseca, and M. Preuss: *Acta Mater.*, 2017, vol. 129, pp. 72–82.
42. F. Hild and S. Roux: *Exp. Mech.*, 2012, vol. 52 (9), pp. 1503–19.
43. F. Hild and S. Roux: *Strain*, 2006, vol. 42 (2), pp. 69–80.
44. J.Q. Da Fonseca, P.M. Mummery, and P.J. Withers: *J. Microsc.*, 2005, vol. 218, pp. 9–21.
45. B. Pan, K. Qian, H. Xie, and A. Asundi: *Meas. Sci. Technol.*, 2009, vol. 20 (10), p. 105002.
46. P.D. Littlewood and A.J. Wilkinson: *Int. J. Fatigue*, 2012, vol. 43, pp. 111–9.
47. D. Lunt, A. Ho, A. Davis, A. Harte, F. Martina, J. Quinta da Fonseca, and P. Prangnell: *Mater. Sci. Eng., A*, 2020, vol. 788, p. 139608.
48. D. Lunt, A. Ho, A. Davis, F. Martina, J. Hönnige, J. Quinta, and P. Prangnell: *MATEC Web Conf.*, 2020, vol. 321, p. 03008.
49. ASTM E8/E8M-11: *Standard Test Methods for Tesnion Testing of Metallic Materials,* ASTM International, West Conshohocklen, PA, 2011.
50. J. Schindelin, I. Arganda-Carreras, E. Frise, V. Kaynig, M. Longair, T. Pietzsch, S. Preibisch, C. Rueden, S. Saalfeld, B. Schmid, J.Y. Tinevez, D.J. White, V. Hartenstein, K. Eliceiri, P. Tomancak, and A. Cardona: *Nat. Methods*, 2012, vol. 9 (7), pp. 676–82.
51. C.A. Schneider, W.S. Rasband, and K.W. Eliceiri: *Nat. Methods*, 2012, vol. 9 (7), pp. 671–75.
52. M.D. Atkinson, R. Thomas, A. Harte, P. Crowther, and J. Quinta da Fonseca: *DefDAP: Deformation Data Analysis in Python*, 2020.
53. F. Gioacchino and J. Quinta da Fonseca: *Exp. Mech.*, 2013, vol. 53 (5), pp. 743–54.
54. D. Lunt, J.Q. da Fonseca, D. Rugg, and M. Preuss: *Mater. Sci. Eng., A*, 2017, vol. 680, pp. 444–53.
55. ASTM Standard E384: *Standard Test Method for Microindentation Hardness of Materials*, ASTM International, West Conshohocken, PA, 2017.
56. K. Zhang, J. Mei, N. Wain, and X. Wu: *Metall. Mater. Trans. A*, 2010, vol. 41A (4), pp. 1033–45.
57. I. Weiss and S.L. Semiatin: *Mater. Sci. Eng., A*, 1999, vol. 263 (2), pp. 243–56.
58. X. Xu, D. Lunt, R. Thomas, R.P. Babu, A. Harte, M. Atkinson, J.Q. Fonseca, and M. Preuss: *Acta Mater.*, 2019, vol. 175, pp. 376–93.

59. Y. Mishin and C. Herzig: *Acta Mater.*, 2000, vol. 48 (3), pp. 589–623.
60. M. Köppers, C. Herzig, M. Friesel, and Y. Mishin: *Acta Mater.*, 1997, vol. 45 (10), pp. 4181–91.
61. F.K. Mante, G.R. Baran, and B. Lucas: *Biomaterials*, 1999, vol. 20 (11), pp. 1051–5.
62. M. Shahedi Asl, A. Sabahi Namini, A. Motallebzadeh, and M. Azadbeh: *Mater. Chem. Phys.*, 2018, vol. 203, pp. 266–73.
63. Y. Yulan, W. Weiqi, L. Fengli, L. Weiqing, and Z. Yongqiang: *Mater. Sci. Forum*, 2009, vol. 618, pp. 169–72.
64. S. Sneddon, D.M. Mulvihill, E. Wielewski, M. Dixon, D. Rugg, and P. Li: *Mater. Charact.*, 2021, vol. 172, p. 110901.

Publisher's Note Springer Nature remains neutral with regard to jurisdictional claims in published maps and institutional affiliations.